Original Article

METTL14 Drives Neuronal Ferroptosis in Spinal Cord Injury by Inducing m6A Methylation of *USP7*

Ke Wang[1,2,3], Jiebin Wang[1,3], Yichi Zhou[1,3], Dingwu Chen[1,3], Jian Wan[1,3], Fanglin Wang[1,3], Zhiqiang Zhang[4,*] and Changsheng Wang[1,2,3,*]

[1]Department of Spinal Surgery, The First Affiliated Hospital, Fujian Medical University, 350005 Fuzhou, Fujian, China
[2]Department of Spinal Surgery, Affiliated Yueqing Hospital of Wenzhou Medical University, 325000 Wenzhou, Zhejiang, China
[3]Department of Spinal Surgery, National Regional Medical Center, Binhai Campus of the First Affiliated Hospital, Fujian Medical University, 350012 Fuzhou, Fujian, China
[4]Fujian Key Laboratory of Natural Medicine Pharmacology, School of Pharmacy, Fujian Medical University, 350122 Fuzhou, Fujian, China

Abstract

Background: Spinal cord injury (SCI) is a devastating disorder in which ferroptosis drives secondary neuronal degeneration. However, whether m6A epitranscriptomic regulation modulates neuronal ferroptosis via specific downstream pathways remains unclear. **Methods:** A rat model of SCI and erastin-induced neuronal ferroptosis *in vitro* were employed. Methyltransferase-like 14 (*METTL14*) expression and global N6-methyladenosine (m6A) levels were assessed, along with ferroptosis-related markers, including glutathione peroxidase 4 (*GPX4*), acyl-CoA synthetase long-chain family member 4 (*ACSL4*), iron accumulation, lipid peroxidation, and mitochondrial ultrastructure. Loss- and gain-of-function approaches were used to evaluate the functional role of *METTL14* and ubiquitin-specific protease 7 (*USP7*). Methylated RNA immunoprecipitation (MeRIP), RNA stability assays, and molecular analyses were conducted to determine m6A modification of *USP7* mRNA and its regulatory consequences. Behavioral assessments were performed to evaluate locomotor recovery after SCI. **Results:** We observed a significant increase in *METTL14* and m6A levels post-SCI, concomitant with key ferroptotic alterations (reduced *GPX4*, elevated *ACSL4*, iron accumulation, lipid peroxidation). *METTL14* knockdown alleviated these pathological features and improved motor function. In neuronal cells, *METTL14* inhibition reversed erastin-induced ferroptosis hallmarks and restored *USP7*/stearoyl-CoA desaturase (*SCD*) expression. Mechanistic studies revealed that *METTL14* mediated m6A-dependent degradation of *USP7* mRNA, thereby suppressing the *USP7-SCD* pathway—a conclusion substantiated by the rescue effect of *USP7* overexpression on *METTL14*-induced ferroptosis. **Conclusions:** This study reveals that *METTL14* promotes neuronal ferroptosis after SCI by degrading *USP7* mRNA via m6A modification, thereby suppressing the *USP7-SCD* axis. This is the first systematic demonstration that the *METTL14–USP7–SCD* axis drives neuronal ferroptosis in a SCI model and highlights this pathway as a promising therapeutic target for SCI.

Keywords: Methyltransferase-like 14, ubiquitin-specific protease 7, N6-methyladenosine, ferroptosis, spinal cord injury.

***Address for correspondence**: Changsheng Wang, Department of Spinal Surgery, The First Affiliated Hospital, Fujian Medical University, 350005 Fuzhou, Fujian, China; Department of Spinal Surgery, Affiliated Yueqing Hospital of Wenzhou Medical University, 325000 Wenzhou, Zhejiang, China; Department of Spinal Surgery, National Regional Medical Center, Binhai Campus of the First Affiliated Hospital, Fujian Medical University, 350012 Fuzhou, Fujian, China. E-mail: wcs@fjmu.edu.cn; Zhiqiang Zhang, Fujian Key Laboratory of Natural Medicine Pharmacology, School of Pharmacy, Fujian Medical University, 350122 Fuzhou, Fujian, China. E-mail: zzq@fjmu.edu.cn.

Copyright policy: © 2026 The Author(s). Published by Forum Multimedia Publishing, LLC. This article is distributed in accordance with Creative Commons Attribution Licence (http://creativecommons.org/licenses/by/4.0/).

Introduction

Spinal cord injury (SCI) is a devastating disorder of the central nervous system, resulting in permanent motor and sensory deficits, profound physical and psychological sequelae, and lifelong disability [1]. Major traumatic causes include traffic collisions, sports-related accidents, and ballistic injuries [2]. Over the past three decades, the global prevalence of SCI has continued to rise, and currently affects more than one million individuals living with paralysis worldwide, thereby places substantial socioeconomic burdens on patients, families, and healthcare systems [3].

Despite decades of research, SCI remains a debilitating condition with limited curative options. The primary in-

jury phase (mechanical damage) is irreversible, but the secondary injury cascade—characterized by ischemia, excitotoxicity, inflammation, oxidative stress, and cell death—offers a window for therapeutic intervention. However, current clinical management primarily focuses on surgical decompression, hemodynamic stabilization, and rehabilitation, none of which directly target the molecular drivers of secondary neurodegeneration. Stem cell-based therapies have emerged as a promising regenerative approach for SCI [4]. Various cell types, including neural stem/progenitor cells (NSCs/NPCs), mesenchymal stem cells (MSCs), and induced pluripotent stem cells (iPSCs), have been shown to promote tissue repair through multiple mechanisms. However, despite encouraging preclinical results, clinical translation of stem cell therapy faces substantial hurdles, including tumorigenic risk, immunological rejection, poor cell survival and integration after transplantation, ethical concerns, and lack of standardized protocols for cell sourcing, delivery timing, and dosing. Consequently, there is an urgent need to identify novel molecular mechanisms that drive secondary injury, particularly those that are druggable and can be selectively manipulated to preserve neuronal function [5].

Pathologically, SCI evolves through sequential phases of ischemia, oxidative stress, and inflammatory activation, ultimately culminating in widespread cellular dysfunction and death. In particular, regulated cell death pathways—such as apoptosis, necroptosis, autophagy, and ferroptosis—orchestrate secondary neurodegeneration and functional decline [6]. Ferroptosis, an iron-dependent form of cell death characterized by uncontrolled lipid peroxidation, exhibits distinct molecular features that differentiate it from other death modalities [7]. Accumulating evidence supports ferroptosis as a critical contributor to neuronal loss in traumatic central nervous system injuries, including SCI [8–10], highlighting its potential as a therapeutic target.

Epitranscriptionally, RNA modifications serve as adaptive sensors of environmental stress. Among these, N6-methyladenosine (m6A) is the most prevalent internal modification in eukaryotic mRNA, playing a pivotal role in regulating transcript stability and influencing cellular pathophysiology [11,12]. Dysregulation of m6A methylation drives pathogenesis and contributes to the development of various diseases, from metabolic disorders to cancers such as cervical carcinoma [13], pancreatitis [14], and kidney disorders [15]. Methyltransferase-like 14 (*METTL14*), a core component of the m6A methyltransferase complex, contributes to tumor progression and metabolic dysregulation [16,17]. Nevertheless, its role in ferroptosis following SCI remains poorly understood.

Ubiquitination dynamics are reversibly modulated by deubiquitinating enzymes (DUBs), and dysregulation of DUB activity is linked to cancer, neurodegeneration, and inflammatory conditions [18–20]. Ubiquitin-specific protease 7 (USP7, also known as *HAUSP*), a cysteine protease within the USP subfamily of DUBs, cleaves polyubiquitin chains to maintain ubiquitin homeostasis. Previous work has shown that *METTL3* modulates spinal cord neuronal apoptosis via m6A-dependent regulation of *Bcl-2* prompting our hypothesis that *METTL14* may likewise regulate *USP7* through m6A methylation [21]. Notably, *USP7* has been reported to modulate ferroptosis in gastric cancer by deubiquitinating stearoyl-CoA desaturase (*SCD*) [22], a key enzyme that influences membrane lipid peroxidation and ferroptotic sensitivity. Furthermore, *SCD* has been implicated in neuronal regeneration processes [23]. However, it remains unclear whether *METTL14*-mediated m6A methylation regulates *USP7* expression and thereby controls *SCD* levels to promote ferroptosis in SCI. Therefore, this study aims to elucidate the functional contribution of *METTL14* to neuronal ferroptosis after SCI, with a focus on its role in mediating m6A-dependent regulation of *USP7*.

Materials and Methods

Animal Models

Male Sprague-Dawley rats (8 weeks old, 200 ± 20 g) were obtained from Beijing HFK BIOSCIENCE Co., Ltd. (China) and acclimatized in a controlled environment (22–24 °C, 45–55% humidity, 12-h light/dark cycle). Standard food and sterilized water were provided ad libitum. All procedures involving animals were conducted in accordance with protocols approved by the Animal Ethics Committee of Fujian Medical University. (No. IACUC FJMU 2025-0183) and were performed according to the National Institute of Health Guide for the Care and Use of Laboratory Animals. One week after animal adaptation and 30 min before operation, a subcutaneous injection of buprenorphine (0.05 mg/kg) was administered to the rats, along with inhalation of 5% isoflurane and an intraperitoneal injection of ketamine (75 mg/kg) and thiazide (10 mg/kg). The tenth thoracic vertebra (T10) was exposed. To establish the spinal cord percussion model, the fully exposed spinal cord was subjected to a controlled impact. A striker rod (10 g) was positioned vertically above the tissue at a height of 10 cm and released to fall freely. This process was controlled by a MEYUE Spinal Cord Injury Instrument Model M5113 (MEYUE, Changsha, Hunan, China). Immediately following impact, hemorrhage and swelling were observed at the strike site on the spinal cord. Whereas, in sham-operated controls, the surgical procedure was limited to exposure of the spinal cord. The wound was then closed in layers using 5-0 sutures. Additionally, to prevent postoperative infection, penicillin (8 U/kg/day) was administered via intraperitoneal injection for three consecutive days. To ensure procedural consistency, all SCI surgeries were performed by a single, designated surgical team. Following successful establishment of the SCI model, rats were randomly assigned into these groups (n = 9 per group): (1) the NC group, sham-operated controls; (2) the SCI group + 7 days, which received injury for 7 days; (3) the SCI group + 28 days, which

received injury for 28 days; (4) the SCI + sh-NC group, injected with a NC Adeno-Associated Virus (AAV) carrying a non-targeting shRNA prior to injury for 28 days; (5) the SCI + *sh-METTL14* group, which underwent *METTL14* knockdown via AAV before SCI induction. Adeno-associated virus treatment was conducted for once before operation. sh-NC, *sh-METTL14*, (10 μL, 1.2 $\times$ 10^{12} vg/mL; HANBio Tech, Shanghai, China) were intrathecally injected through lumbar puncture. This study was reported in accordance with the ARRIVE guidelines.

Basso, Beattie, Bresnahan (BBB) Evaluation of Locomotion

Hindlimb motor function was assessed in a blinded manner by three independent observers. Evaluations occurred on post-injury days 1, 3, 7, 14, 21, and 28, employing a 21-point scale where 0 represented complete paralysis and 21 represented normal locomotion. The final score for each animal was derived from the average of the three observers' ratings.

Inclined Plane Test (IPT)

In IPT, rats were positioned on a smooth, adjustable inclined plane. Starting at 0°, the plane's angle was gradually elevated in 5–10° steps. The endpoint was recorded as the steepest angle a rat could sustain without falling for a duration of 10 seconds.

Histological Experiment

All rats were euthanized via intraperitoneal injection of a lethal dose of pentobarbital on the 7th, 28th day after operation. A 2-cm segment of spinal cord tissue, centered on the injury epicenter, was dissected and fixed in paraffin. Following embedding, the tissue block was transversely sectioned at equal intervals. Additionally, 5-μm-thick sections from regions equidistant to the lesion site were prepared and subjected to hematoxylin and eosin (HE) staining for histological analysis (Servicebio Tech, Wuhan, China). To evaluate neuronal survival, transverse sections adjacent to the injured site were processed for Nissl staining (Servicebio Tech, Wuhan, China), which included a pretreatment step with 0.1% glacial acetic acid. For iron deposition analysis, sections were subjected to Prussian blue staining. Specifically, a working solution was freshly prepared by mixing equal volumes of 2% potassium ferrocyanide and 2% hydrochloric acid. Sections were immersed in this solution for 30 minutes, followed by two washes with distilled water. And then sections were stained with DAB solution for about 5–10 minutes. Hematoxylin dye staining for 1 min, tap water washing. The sections were observed under a microscope and photographed for DAB-Perls staining, and iron-positive cells were counted (Servicebio Tech, Wuhan, China).

Western Blot

Total protein was extracted from PC12 cells and spinal cord tissues by homogenization in RIPA lysis buffer (P0039, Beyotime, Nanjing, China) supplemented with both protease and phosphatase inhibitor cocktails (HY-K0010, MedChemExpress, Shanghai, China). Protein concentration was subsequently determined using a BCA assay kit (Biosharp, Hefei, China). Subsequently, the protein samples were separated with 10% sodium dodecyl sulfate-polyacrylamide gel electrophoresis (SDS-PAGE) (Beyotime, Nanjing, China) and transferred onto polyvinylidene fluoride (PVDF) membranes (3010040001, Merck, Darmstadt, Germany). After blocking with 5% nonfat milk, the membranes were added with diluted primary antibodies *METTL14* (48699, 1:1000; CST, Massachusetts, USA), *USP7* (ab108931, 1:1000; Abcam, Boston, USA), glutathione peroxidase 4 (*GPX4*; ab125066, 1:1000; Abcam, Boston, USA), acyl-CoA synthetase long-chain family member 4 (*ACSL4*; ab155282, 1:2000; Abcam, Boston, USA), *SCD* (ab236868, 1:1000; Abcam, Boston, USA), and Glyceraldehyde- 3-phosphate dehydrogenase (*GAPDH*; 10494-1-AP, 1:1000; Proteintech, Wuhan, China) and incubated at 4 °C overnight. After washing the membranes, HRP-linked anti-rabbit secondary antibody (7074, 1:2000; CST, Massachusetts, USA) was added and incubated for 1 h. Protein bands were visualized and captured using a ChemiDoc MP+ Imaging System (ChemiDoc, Bio-Rad). Band intensities were subsequently quantified with ImageJ software version 1.53c (U.S National Institutes of Health, Bethesda, MD, USA). All experiments were independently replicated a minimum of three times.

Reverse Transcription-Quantitative Polymerase Chain Reaction (RT-qPCR)

Total RNA was isolated from samples using TRIzol reagent (15596026, Invitrogen, California, USA). Following cDNA synthesis with the HiScript II Q RT SuperMix kit (R223, Vazyme, Nanjing, China), quantitative PCR (Lightcycler 96, Roche, Switzerland) was performed using ChamQ Universal SYBR qPCR Master Mix (Q312, Vazyme, Nanjing, China) and gene-specific primers. Gene expression levels were calculated using the $2^{-\Delta\Delta CT}$ method, with *GAPDH* serving as the endogenous control. The sequences of all primers used are listed below:

USP7 forward primer, 5′-ACCAGGGTGAGCATTTCAGAG-3′ and *USP7* reverse primer, 5′- AGGATGAGACATGTTACCAGGTTG-3′;

METTL14 forward primer, 5′-GCTCTGGGGAAGGATTGGAC-3′ and *METTL14* reverse primer, 5′- CATCTGTGCTTCGCTTCACG′;

GPX4 forward primer, 5′-GGCAGGAGCCAGGAAGTAAT-3′ and *GPX4* reverse primer, 5′- TGGGCATCGTCCCCATTTAC-3′;

SCD forward primer, 5′-

GTTCGTCAGCACCTTCTTGAGAT-3′ and *SCD* reverse primer, 5′- CACTGGCAGAGTAGTCGTAGG-3′;

GAPDH forward primer, 5′-ACGGCAAGTTCAACGGCACAG-3′ and *GAPDH* reverse primer, 5′-GAAGACGCCAGTAGACTCCACGAC-3′.

Global m6A Measurement

Global m6A levels in total RNA were assessed using an m6A-specific quantification kit (P-9005-96, Epigentek, New York, USA). In brief, 200 ng of RNA per well was subjected to the capture and detection steps as outlined in the kit manual. Quantification was performed by interpolating values from a parallel standard curve.

Immunohistochemical Staining

To minimize background, tissue sections were first treated with an auto-fluorescent quencher. They were then blocked by applying normal goat serum for 30 minutes at room temperature. After removing the blocking solution by blotting, slides were incubated with primary antibodies against *METTL14* (1:6000, GB114688; Servicebio Tech, Wuhan, China), *NeuN* (1:5000, GB11538; Servicebio Tech, Wuhan, China), and *GPX4* (1:5000, GB120010; Servicebio Tech, Wuhan, China) at 4 °C overnight. The following day, slides were rinsed three times with PBS (phosphate-buffered saline, 3 min per wash) and subsequently probed in the dark with fluorescent secondary antibodies (488/647/555-conjugated goat anti-mouse/rabbit IgG, 1:500, Servicebio GB23303/GB23301; Servicebio Tech, Wuhan, China) at 37 °C for 1 hour. Following another three PBS washes in the dark, nuclei were counterstained with DAPI (1:500, G1012; Servicebio Tech, Wuhan, China) for 5 minutes. After a final PBS wash, slides were mounted and images were acquired using a Nikon fluorescence microscope (NIKON Eclipse Ci; Nikon, Tokyo, Japan).

Cell Culture and Treatment

Highly differentiated PC12 cells (rat pheochromocytoma cell line; Procell, Wuhan, China) were cultured in RPMI 1640 medium (C11875500BT, Gibco, New York, USA) supplemented with 10% fetal bovine serum (ST30-3302, PAN, Aidenbach, Germany) and 1% penicillin/streptomycin (C0222, Beyotime, Nanjing, China) at 37 °C in a humidified 5% CO_2 incubator, with medium replenished every two days. To model ferroptosis *in vitro*, cells at 60–80% confluence were treated with erastin (E424821, Aladdin, Shanghai, China), while ferrostatin-1 (F408509, Aladdin, Shanghai, China) was used as an inhibitor in control groups. Subsequent analyses were performed following the indicated treatments.

Cell Viability Assays

To assess cytotoxicity, PC12 cell viability was determined via a Cell Counting Kit-8 (CCK-8) assay (AR1160-500, Boster, Wuhan, China). Briefly, cells were seeded into 96-well plates at 6×10^3 cells/well in 100 μL medium and allowed to adhere overnight. They were then exposed to a concentration gradient of erastin or vehicle (DMSO) for 24 h. Subsequently, the medium in each well was replenished with 100 μL of fresh medium containing 10% (v/v) CCK-8 reagent. Following a 2-hour incubation at 37 °C, the absorbance at 450 nm was measured using a microplate reader (51119080, Thermo, Massachusetts, USA). Viability was calculated as a percentage relative to the control group.

Cellular Iron, Malondialdehyde (MDA), glutathione (GSH) Measurement

Several oxidative stress-related biomarkers were assessed with colorimetric kits: iron content was measured with an Iron Assay Kit (S1066M, Beyotime, Nanjing, China); lipid peroxidation was evaluated by detecting MDA levels using an MDA assay kit (S0131M, Beyotime, Nanjing, China); and GSH levels were determined with a GSH assay kit (S0053, Beyotime, Nanjing, China). All procedures followed the kit manuals.

Transmission Electron Microscope

Mitochondrial ultrastructure was examined by transmission electron microscopy (TEM). PC12 cells, after receiving the indicated treatments, were processed for TEM as follows: primary fixation in 2.5% glutaraldehyde for 2 h, followed by post-fixation in 1% osmium tetroxide for another 2 h, both at room temperature. Samples were then dehydrated through a graded ethanol series (30%, 50%, 70%, 80%, 95%, and 100%; 20 min per step) and embedded in EMBed 812 resin. Ultrathin sections were prepared, stained successively with uranyl acetate and lead citrate, and imaged using a Hitachi H-7800 (Tokyo, Japan) transmission electron microscope.

Cell Transfection

When PC12 cells reached 50% confluency in the 6-well plates, cells were transfected with 2 μg shRNA of *METTL14* (*sh-METTL14*) or its shRNA NC (sh-NC), shRNA of *USP7* (LV-*USP7*) or its NC (LV-NC) at 37 °C for 48 h and then screened with 4 μg/ml of puromycin (C8156, Adamas, Shanghai, China) for ≥5 days. While transfected with 4 μg overexpression plasmid of *METTL14* (oe-*METTL14*) or its NC (oe-NC), 50 nM siRNA of *USP7* or its inhibitor NC (Si-NC) at 37 °C for 12 h using Lipofectamine®3000 (Invitrogen, California, USA). PC12 cells were collected for RT-qPCR and western blot to detect transfection efficiency of *METTL14* and *USP7*. The shRNA targeting *METTL14* (*sh-METTL14*), lentiviral vector overexpressing *USP7* (*LV-USP7*), and their corresponding negative controls were obtained from Shanghai GeneChem Co., Ltd. (Shanghai, China). The siRNA tar-

geting *USP7* and its negative control were purchased from HanBio Technology Co., Ltd. (Shanghai, China).

Bioinformatics Analysis

Bioinformatics analyses were performed to investigate *METTL14*'s role. The m6A modification profile and secondary structure of *USP7* mRNA were predicted via the SRAMP database. To identify *METTL14* binding targets, we interrogated the RMBase v2.0 database, which also revealed the predominant m6A consensus motifs. Finally, the specific binding region between *METTL14* and *USP7* mRNA was predicted using the catRAPID omics v2.0 tool.

m6A-RNA Immunoprecipitation Assay

The interaction between *METTL14* and target RNAs, as well as their m6A modification status, were analyzed by RNA immunoprecipitation using BersinBio^{TM} kits (RIP: Bes5101; MeRIP: Bes5203-2, Guangzhou, China). The protocol involved incubating cell lysates with magnetic beads pre-bound with the relevant antibody. Immunoprecipitated RNA was subsequently isolated, and the expression levels of specific genes were quantified via RT-qPCR to assess enrichment.

RNA Stability Detection

After treatment with 5 μg/ml Actinomycin D (50-76-0, Aladdin, Shanghai, China), the cells were incubated for 0, 2, 4, 6 and 8 hours, after which they were harvested for RNA extraction using TRIzol reagent as described previously. Subsequently, the rate of mRNA degradation was determined based on methods outlined in the published literature.

Dihydroethidium (DHE) Staining

DHE fluorescence staining was performed to evaluate intracellular reactive oxygen species (ROS) production according to the manufacturer's protocol. After a PBS wash, sections were incubated with 5 μM DHE (S0064S, Beyotime, Nanjing, China) under light-protected conditions at 37 °C for 30 min. Fluorescent signals were examined and captured prior to imaging with a Zeiss fluorescence microscope (Zeiss, Heidenheim, Germany).

Flow Cytometry

Cells were collected into flow tubes and centrifuged to discard the supernatant. Mitochondrial membrane potential was detected with instructions of JC-1 (C2005, Beyotime, Nanjing, China). Flow cytometric analysis was performed with BD FACSCanto (BD, New York, USA) flow cytometers. Data were analyzed with FlowJo v10.6.2 software.

Co-Immunoprecipitation (Co-IP) and Ubiquitination Assay

Co-IP extracts were prepared using IP lysis buffer (P0013, Beyotime, Nanjing, China) supplemented with protease inhibitor cocktails (P1005, Beyotime, Nanjing, China). These protein solutions were then incubated with at 4 °C with 3–5 μL primary antibody for 6 h. After washing three times using lysis buffer, protein A/G magnetic beads (HY-K0202, MCE, New York, USA) were added to the protein-antibody mixture, and the protein-antibody-magnetic bead mixture was shaken moderately at 4 °C for 6 h. After washing with lysis, the bound proteins were eluted with 1× protein loading buffer at 95 °C for 10 min and analyzed by Western blot and ubiquitination assay.

Statistical Analysis

All behavioral, histological, and molecular analyses were conducted by investigators blinded to the experimental groups. Statistical analyses were conducted using SPSS 22.0 (SPSS Inc., Chicago, IL, USA) and GraphPad Prism 8.0 (GraphPad, San Diego, CA, USA) Continuous data are expressed as means ± standard deviation (SD). For comparisons between two groups, Student's t-test was used. Comparisons among multiple groups were performed by one-way or two-way analysis of variance (ANOVA), as appropriate, with Tukey's post hoc test for subsequent pairwise comparisons. Correlations were analyzed using Pearson's coefficient. All tests were two-tailed, and a p-value < 0.05 was considered statistically significant.

Results

METTL14-Mediated m6A Modification Was Involved in SCI

As the most abundant RNA methylation modification, m6A regulates gene expression through multifaceted control of mRNA processing. To investigate its role in SCI, we established a rat SCI model and serially assessed motor function using BBB scores and inclined plane testing at postoperative days 1, 3, 7, 14, 21, and 28. Rats developed immediate hindlimb paralysis following injury, and a slight but significant increase in BBB scores was detected from day 3 post-injury (Fig. 1**A**,**B**). Histopathological evaluation of spinal cord tissues at day 28 revealed extensive destruction of both gray and white matter, accompanied by significant loss of anterior horn motor neurons (Fig. 1**C**). Global m6A levels, as measured by Epiquik m6A quantification assay, were significantly elevated in spinal cord tissues of SCI rats across multiple time points (Fig. 1**D**). Given that *METTL14*—a core component of the m6A methyltransferase complex—has been reported to promote ferroptosis in cervical cancer via m6A methylation [13,24]. We hypothesized that it may also participate in SCI pathogenesis. Consistent with this, triple-method validation (RT-qPCR, Western blot, and immunofluorescence) confirmed substantial upregulation of *METTL14* in day-28 SCI tissues, with immunofluorescence intensity markedly increased compared to sham controls (Fig. 1**E–I**). Elevated *METTL14* fluorescence intensity was associated with a reduced number of *NeuN*-positive neurons in the injured

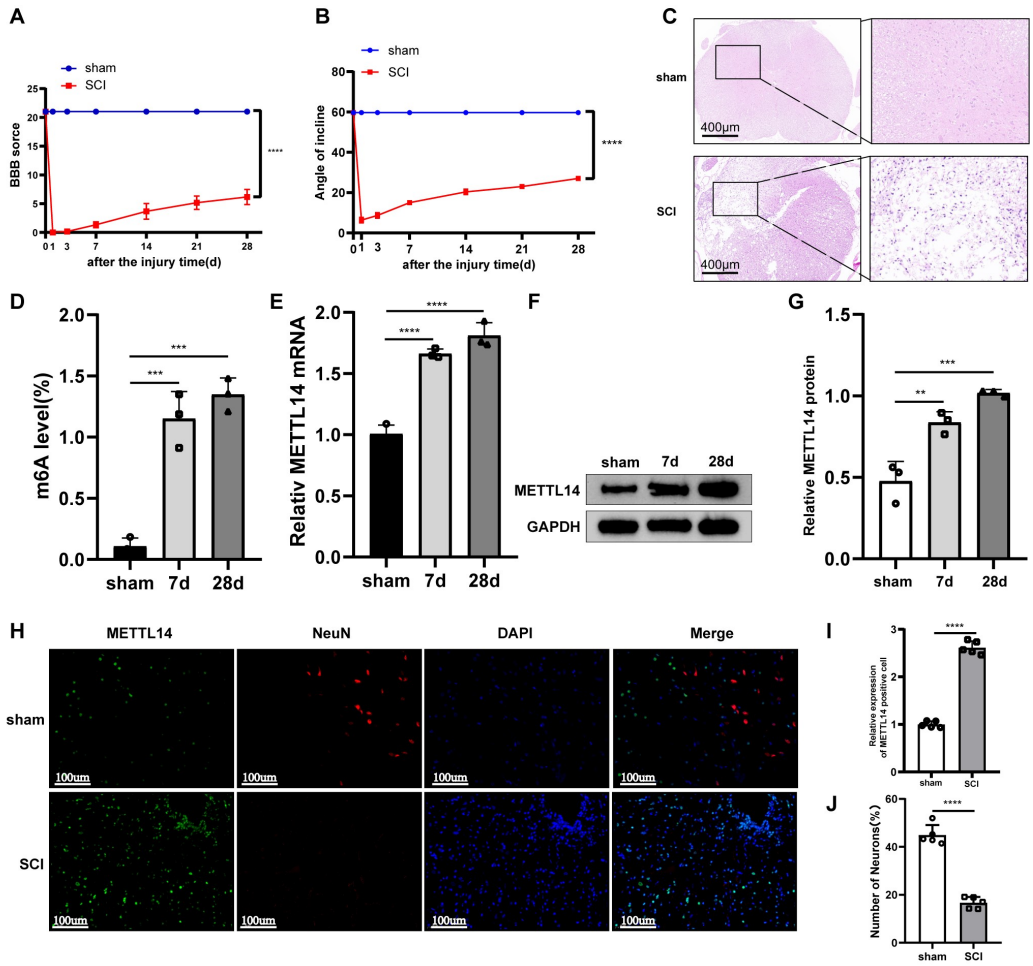


Fig. 1. ***METTL14*** **and m6A were significantly upregulated after SCI.** (**A,B**) On post-operative days 1, 3, 7, 14, 21, and 28, the locomotor function of all rats was serially evaluated using the Basso, Beattie, Bresnahan (BBB) open-field locomotor scale in combination with the inclined plane test. (**C**) HE staining analysis of day-28 spinal cord tissues. (**D**) m6A levels in SCI rat spinal cords. (**E–I**) Quantitation of RT-qPCR, Western blot, immunofluorescence of *METTL14* in SCI tissues. (**H,J**) Immunofluorescence staining for *NeuN* on the 28th day after SCI. The data in the figures represent the means ± SD. Pairwise comparisons were analyzed using independent *t*-test. Significant differences between groups are indicated as ****$p < 0.0001$, ***$p < 0.001$, **$p < 0.01$. The figures were drawn using Adobe Illustrator 2022.

spinal cord (Fig. 1**H–J**). Together, these results indicate concomitant upregulation of *METTL14* and m6A methylation following SCI, suggesting their potential involvement in the underlying molecular pathology.

Neurons Suffer From Ferroptosis in Rat After SCI

Consistent with established findings [25,26], we confirmed pathological activation of ferroptosis in our SCI rat model. Western blot analysis revealed aberrant expression of key ferroptosis markers: significant downregulation of *GPX4* accompanied by concurrent upregulation of *ACSL4* in SCI tissues compared to sham controls (Fig. 2**A**,**B**). Biochemical assays demonstrated substantially elevated iron accumulation and MDA levels in SCI versus sham groups (Fig. 2**C**,**D**). Histological assessment using DAB-Perls staining showed abundant iron-positive cells in SCI lesions, in sharp contrast to the minimal iron deposition observed in sham tissues (Fig. 2**E**). Furthermore, immunofluorescence analysis confirmed markedly reduced *GPX4* expression in spinal cord neurons of SCI rats (Fig. 2**F**,**G**). Collectively, these multi-methodological approaches provide convergent evidence confirming ferroptosis activation during SCI pathogenesis, supported by histological, biochemical, and molecular evidence.

shRNA-METTL14 Inhibited SCI Progression and Promoted the Recovery of Motor Function After SCI in Rat

To elucidate the functional impact of *METTL14* in SCI, we performed intrathecal injection of an AAV vector encoding shRNA targeting *METTL14*. The successful knockdown of *METTL14* expression was confirmed at both protein and mRNA levels by Western blot and RT-qPCR analyses, respectively (Fig. 3**A–C**). Behavioral assessments revealed substantial functional recovery in *sh-*

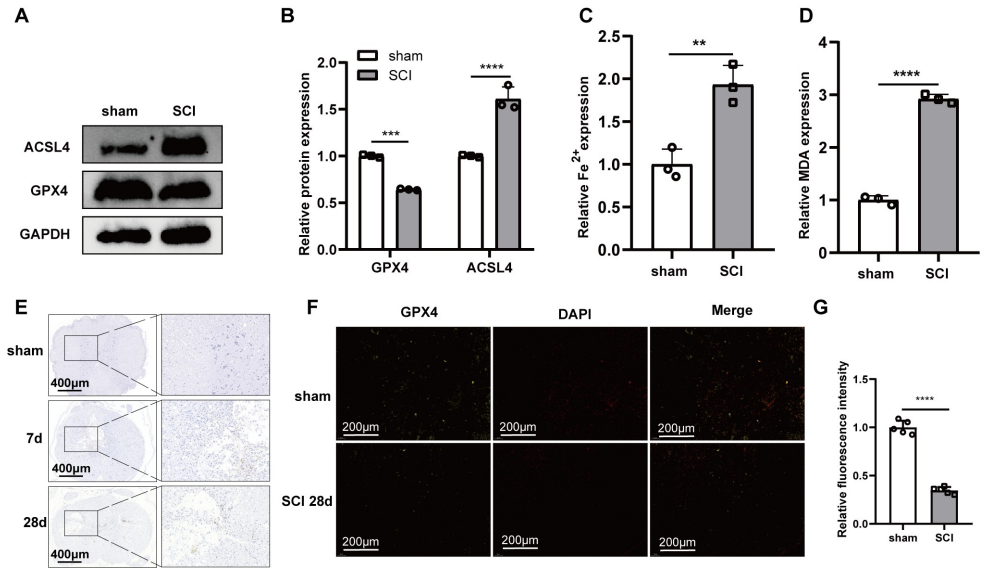


Fig. 2. Neurons suffer from ferroptosis in rat after SCI. (**A,B**) Quantitation of Western blot of *GPX4* and *ACSL4* in SCI tissues. (**C,D**) Fe^{2+} and MDA measurement. (**E**) On the 7th and 28th after SCI, DAB-Perls staining was used to reveal pathological changes of spinal cord. (**F,G**) Fluorescence intensity of immunofluorescence staining of *GPX4*. The data in the figures represent the means ± SD and analyzed using independent *t*-test. Significant differences between groups are indicated as ****$p < 0.0001$, ***$p < 0.001$, **$p < 0.01$. The figures were drawn using Adobe Illustrator 2022.

METTL14 rats, with significantly improved BBB scores and inclined plane performance at day 28 post-SCI (Fig. 3**D,E**). Footprint analysis further demonstrated enhanced gait recovery and motor coordination in *sh-METTL14* rats versus sh-NC controls (Fig. 3**G**). Global m6A levels in spinal cord tissues were significantly reduced following *METTL14* knockdown (Fig. 3**F**). Histological examination showed attenuated gray and white matter destruction, with greater anterior horn neuron survival in *sh-METTL14* rats compared to sh-NC controls (Fig. 3**H**). These findings demonstrate that *METTL14* knockdown mitigates SCI pathology and promotes functional recovery through m6A-dependent mechanisms.

shRNA-METTL14 Inhibited Ferroptosis of Spinal Neurons in SCI Rats

To delineate the role of *METTL14* in neuronal ferroptosis following SCI, we conducted multiplex immunofluorescence staining for *METTL14*, *GPX4*, and the neuronal marker *NeuN* in spinal cord tissues at day 28 post-injury (Fig. 4**A**). *METTL14* knockdown significantly reduced *METTL14*-positive cells while increasing the number of neurons (Fig. 4**B**,**D**). Concomitantly, *GPX4* fluorescence intensity increased in *shRNA-METTL14*+SCI versus sh-NC+SCI (Fig. 4**C**). DAB-Perls staining revealed the number of iron-positive cells in the *shRNA-METTL14*+SCI group decreased significantly (Fig. 4**E**). In addition, biochemical assays confirmed decreased iron content and MDA levels in *shRNA-METTL14*+SCI spinal cords (Fig. 4**G**,**H**). Nissl staining revealed significantly enhanced neuronal survival in the ventral horns of *shRNA-METTL14*+SCI rats (Fig. 4**F**). These results collectively demonstrate that *METTL14* knockdown effectively attenuates ferroptotic damage and promotes neuronal survival in the injured spinal cord.

METTL14 Knockdown Inhibited Erastin-Induced Ferroptosis in Cell Model

To further elucidate the molecular mechanism by which *METTL14* regulates ferroptosis in SCI, we established an *in vitro* ferroptosis model using erastin-treated PC12 neuronal cells. Dose-response analysis via CCK-8 assays determined an IC_{50} of 11.02 μM for erastin (24 h exposure; Fig. 5**A**), leading to the selection of 10 μM for subsequent experiments. *METTL14* expression was effectively knocked down using specific shRNAs, as confirmed by both Western blot and RT-qPCR analyses (Fig. 5**B–D**). Silencing *METTL14* significantly rescued erastin-induced viability loss in PC12 cells, as evidenced by CCK-8 assays (Fig. 5**E**). Erastin treatment significantly elevated m6A levels, iron content, and MDA production while depleting GSH (Fig. 5**F–I**). *METTL14* knockdown or ferrostatin-1 (Fer-1) treatment partially reversed these erastin-induced alterations, restoring m6A, MDA, and iron to near-basal levels while rescuing GSH depletion. Western blot analysis demonstrated that METTL14 silencing prevented erastin-induced *GPX4* suppression (Fig. 5**J,K**). Mitochondrial morphological analysis revealed that *METTL14* down-regulation significantly attenuated erastin-induced mitochondrial shrinkage and membrane density increase (Fig. 5**L**). Collectively, these findings indicate that *METTL14* knockdown attenuates ferroptosis in erastin-treated neu-

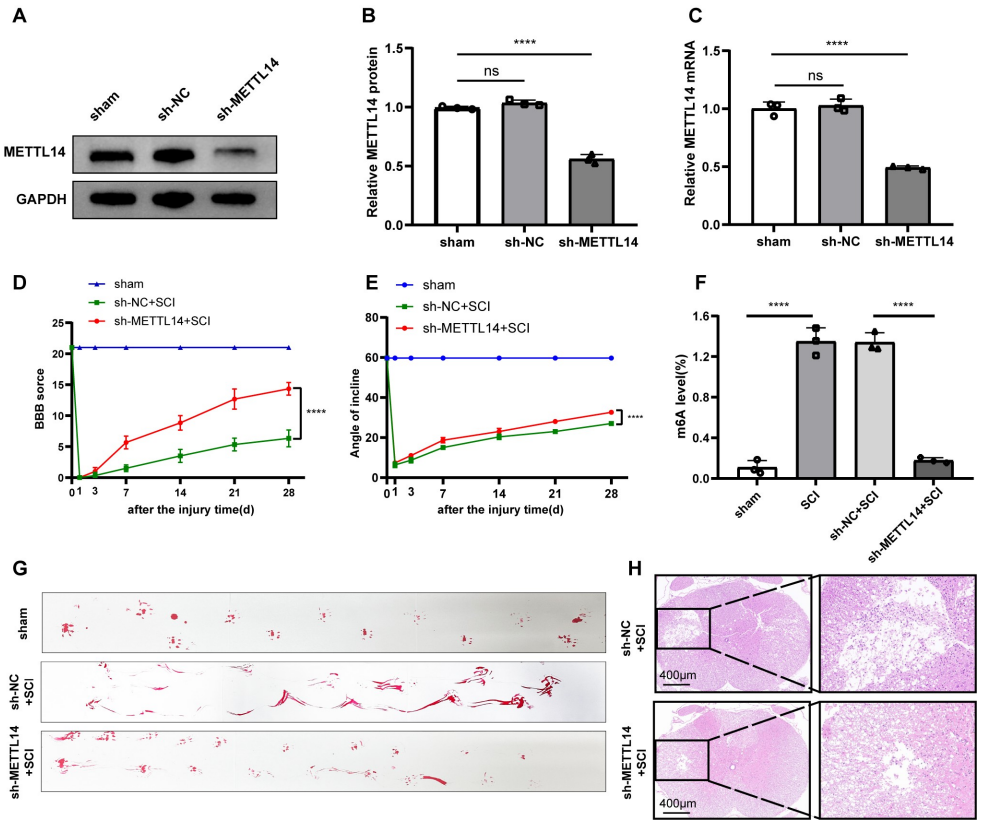


Fig. 3. *ShRNA-METTL14* inhibited SCI progression and promoted the recovery of motor function after SCI in rat. (**A-C**) Western blot and RT-qPCR were used to detect *METTL14* in SCI tissues. (**D,E**) BBB motor function score and inclined plane test score. (**F**) m6A levels in SCI rat spinal cords. (**G**) Footprint test on the 28th after SCI. (**H**) HE staining analysis of day-28 spinal cord tissues. The data in the figures represent the means ± SD and analyzed using independent *t*-test. Significant differences between groups are indicated as ****$p < 0.0001$. The figures were drawn using Adobe Illustrator 2022.

ronal cells through m6A-dependent mechanisms, suggesting *METTL14* as a potential therapeutic target for mitigating ferroptotic damage in SCI.

USP7 Was Identified to be Target for METTL14 in Ferroptosis

As a key cysteine peptidase within the USP subfamily of DUBs, ubiquitin-specific protease 7 (*USP7*) governs ubiquitination dynamics, playing a pivotal role in the pathogenesis of SCI [27]. Analysis of spinal cord tissues from SCI rats revealed significant upregulation of *USP7* at both mRNA and protein levels compared to sham controls (Fig. 6**A,B**). Given *METTL14*'s established function as an m6A methyltransferase regulating mRNA stability [24]. We computationally predicted m6A modification sites within the *USP7* transcript using the SRAMP database. Bioinformatic analysis identified three high-confidence m6A motifs in the 3'UTR region, coinciding with areas of high mRNA structural flexibility (Fig. 6**C,D**). Based on these findings, we hypothesized that *METTL14* regulates *USP7* expression via m6A-dependent mechanisms. Experimental validation through RNA immunoprecipitation (RIP) and MeRIP-qPCR assays confirmed that *METTL14* knockdown significantly reduced both m6A modification levels and *METTL14* binding enrichment on USP7 mRNA (Fig. 6**E,F**). To further assess the functional consequences of this interaction, we evaluated *USP7* mRNA stability and found that *METTL14* inhibition substantially prolonged *USP7* mRNA half-life (Fig. 6**G**). Consequently, *METTL14* inhibition elevated *USP7* expression at both transcriptional and translational levels compared to sh-NC groups (Fig. 6**H–J**). In summary, our results demonstrate that *METTL14* directly interacts with *USP7* mRNA and catalyzes its m6A modification, thereby establishing *METTL14* as the writer enzyme responsible for post-transcriptional regulation of *USP7* in the context of SCI.

USP7 Regulates SCD Expression Through Deubiquitination in Ferroptosis

SCD, a key enzyme in monounsaturated fatty acid biosynthesis, critically regulates lipid peroxidation and ferroptosis susceptibility [28]. Genetic or pharmacological inhibition of *SCD* enhances lipid peroxidation and sensitizes cells to ferroptosis, whereas *SCD* overexpression confers cellular protection [29,30]. These findings align with previous reports that USP7 inhibition induces ferroptosis in gastric cancer by targeting *SCD* [22]. To validate the regulatory role of *USP7* on *SCD* in neuronal ferroptosis,

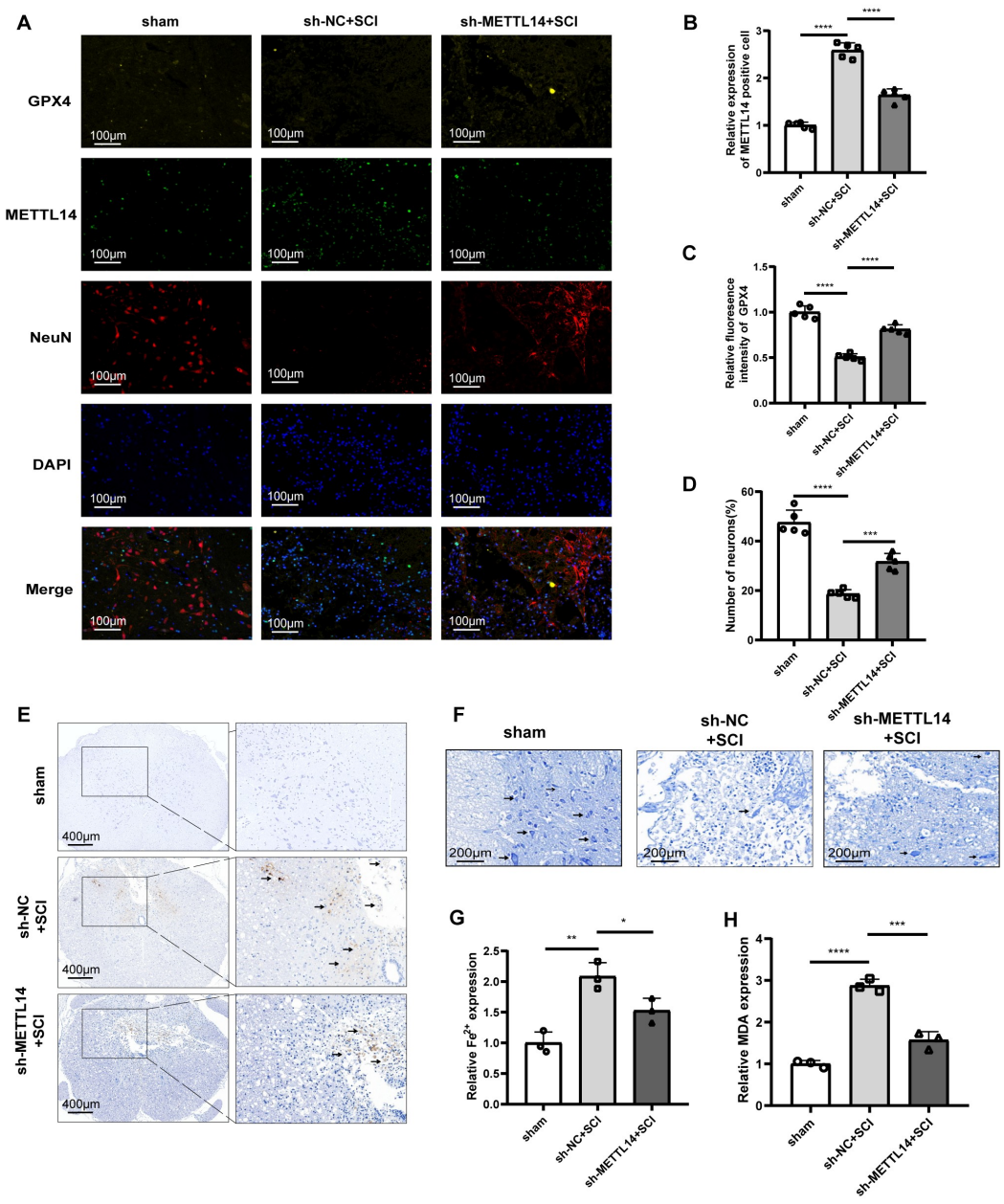


Fig. 4. *ShRNA-METTL14* inhibited ferroptosis of spinal neurons in SCI rats. (**A–D**) Multiplex immunofluorescence staining for *METTL14*, *GPX4*, *NeuN* on the 28th day after SCI. (**E,F**) DAB-Perls staining and Nissl staining were used to reveal pathological changes of spinal cord on the 28th day after SCI in different groups. (**G,H**) Fe^{2+} and MDA measurement. The data in the figures represent the means ± SD and analyzed using independent *t*-test. Significant differences between groups are indicated as ****$p < 0.0001$, ***$p < 0.001$, **$p < 0.01$, *$p < 0.05$. The figures were drawn using Adobe Illustrator 2022.

we first overexpressed *USP7* in PC12 cells using lentiviral delivery, which was confirmed by Western blot and RT-qPCR (Fig. 7**A,B**). In erastin-treated neuronal cells, we found that *USP7* overexpression significantly restored the expression of *GPX4* (Fig. 7**C**). Co-immunoprecipitation assays demonstrated a direct physical interaction between *USP7* and *SCD* (Fig. 7**D,E**). Importantly, *USP7* overexpression significantly reduced the ubiquitination level of *SCD* in erastin-treated PC12 cells (Fig. 7**F**). Erastin challenge markedly downregulated *SCD* protein expression

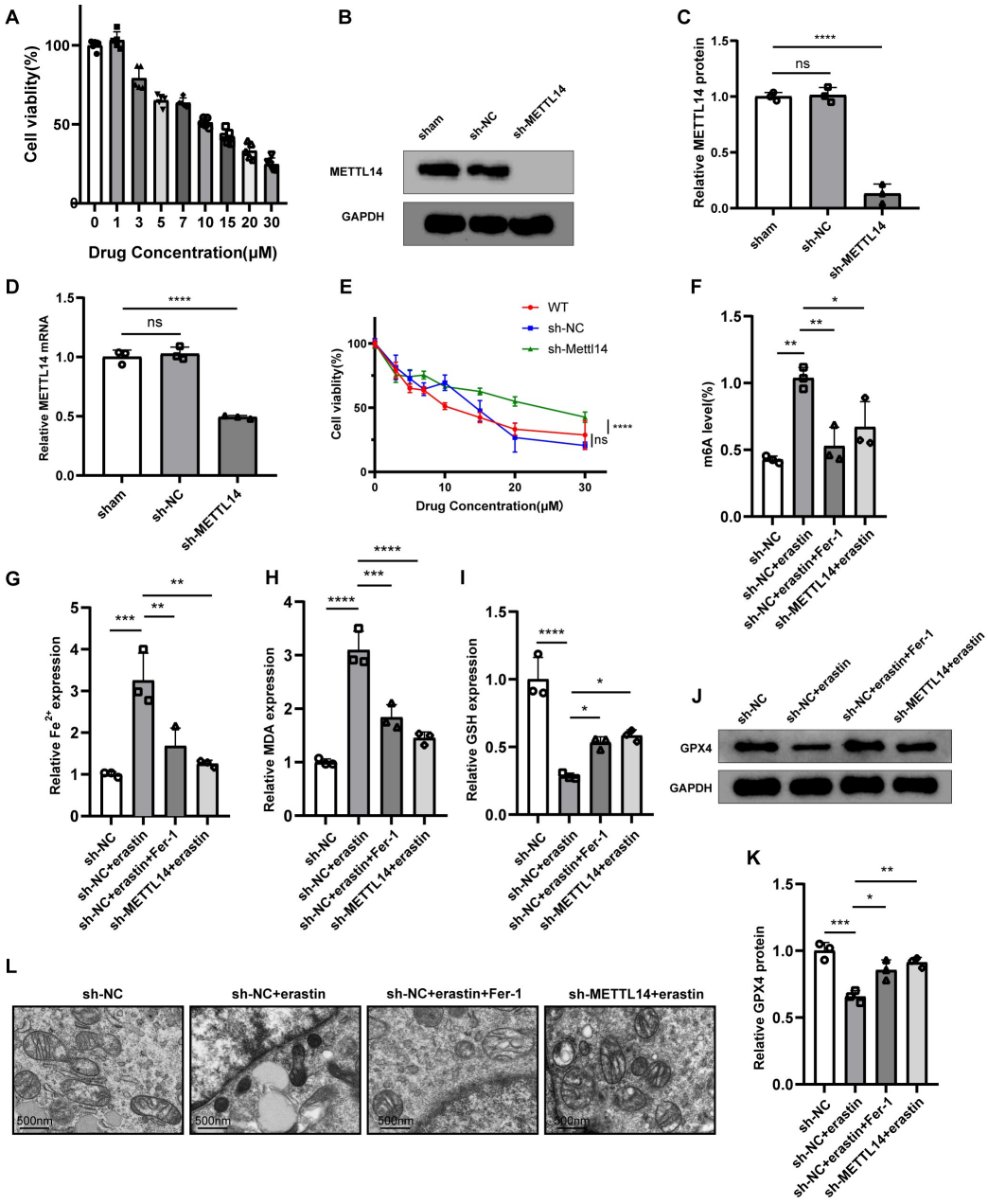


Fig. 5. *METTL14* knockdown inhibited erastin-induced ferroptosis in cell model. (**A**) CCK-8 assays were used to detect the IC_{50} of erastin in PC12 cells. (**B–D**) Western blot and RT-qPCR were used to detect *METTL14* in PC12 cells. (**E**) Cell viability was verified using CCK-8 assays. (**F**) m6A levels in PC12 cells. (**G-I**) Fe^{2+}, MDA, GSH measurement. (**J,K**) Expression of *GPX4* in cells by Western blot. (**L**) Mitochondrial morphology alterations in cells were evaluated by TEM. The data in the figures represent the means ± SD and analyzed using independent *t*-test. Significant differences between groups are indicated as ****$p < 0.0001$, ***$p < 0.001$, **$p < 0.01$, *$p < 0.05$. The figures were drawn using Adobe Illustrator 2022.

(Fig. 7**G–I**). Conversely, siRNA-mediated knockdown of *USP7* (Fig. 7**J–L**) led to a corresponding decrease in *SCD* protein levels (Fig. 7**M,N**). In summary, these results establish that USP7 deubiquitinates and stabilizes *SCD*, thereby modulating ferroptosis execution in neuronal cells.

Overexpression of USP7 Effectively Counteracted the Influence of oe-METTL14 on the Ferroptosis of SCI Cells

These results confirm that *METTL14* exacerbates SCI by mediating m6A-dependent suppression of *USP7* expression, which in turn inhibits *SCD* and promotes ferroptosis. To functionally validate this regulatory axis, PC12 cells were co-transfected with METTL14-overexpressing (*oe-METTL14*) and *USP7*-overexpressing (*LV-USP7*) constructs, followed by erastin treatment to induce ferropto-

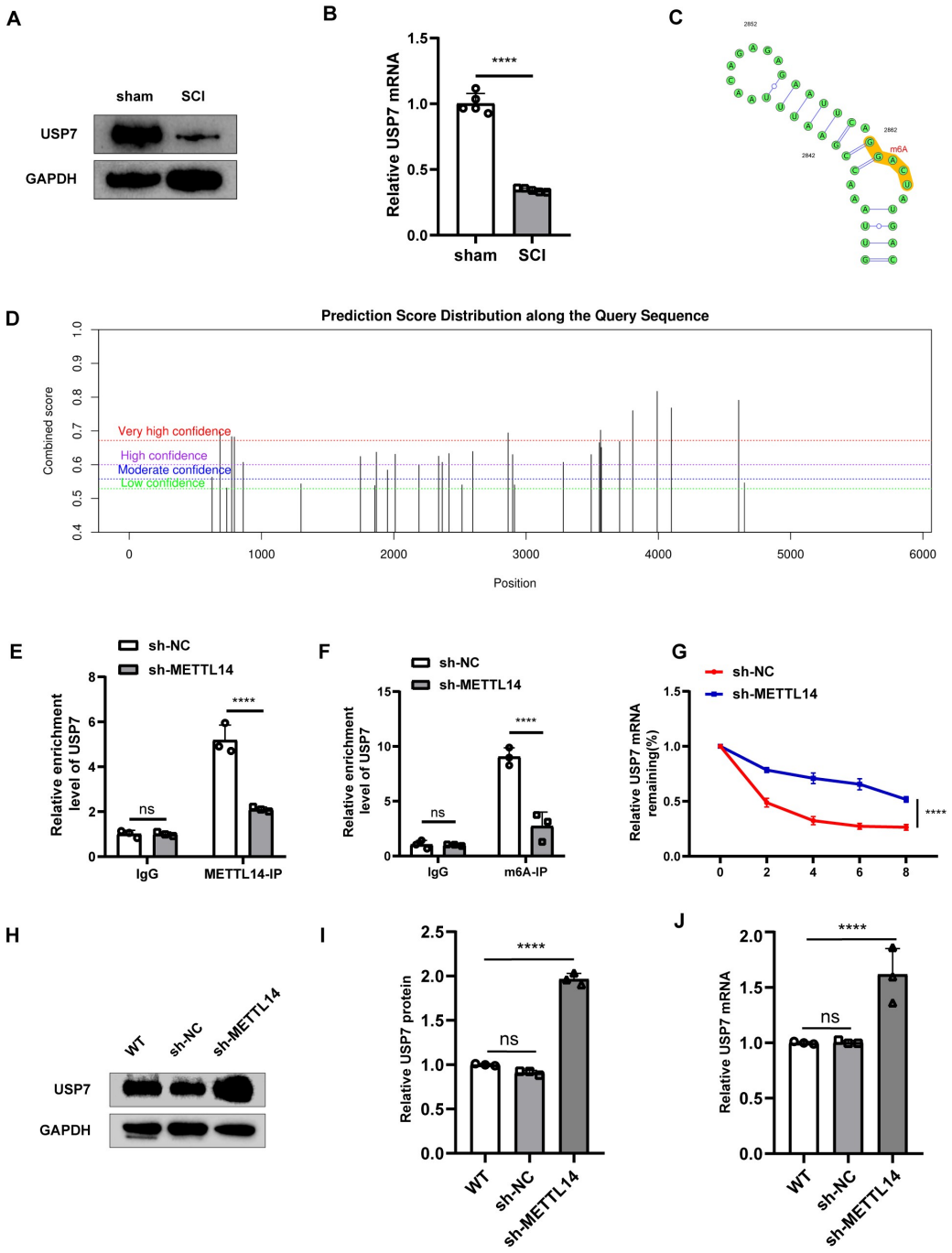


Fig. 6. *USP7* was identified to be target for *METTL14* in ferroptosis. (**A,B**) Expression of *USP7* by Western blot and RT-qPCR in SCI tissues. (**C**) The distribution of m6A modification on *USP7* mRNA. (**D**) The secondary structure of *USP7* mRNA. (**E**) RIP shows that *METTL14* interacts with *USP7* mRNA. (**F**) MeRIP shows the presence of m6A modification of *USP7* mRNA. (**G**) Detection of *USP7* mRNA stability by RT-qPCR in PC12 cells. (**H–J**) Expression of *USP7* in cells by Western blot and RT-qPCR. The data in the figures represent the means ± SD and analyzed using independent *t*-test. Significant differences between groups are indicated as ****$p < 0.0001$. The figures were drawn using Adobe Illustrator 2022.

sis (Fig. 8**A–C**). Western blot analysis revealed that co-expression of *oe-METTL14* and *LV-USP7* significantly restored protein levels of both *GPX4* and *USP7* compared to the *oe-METTL14*-only group (Fig. 8**D–F**). Furthermore, cells overexpressing *METTL14* alone exhibited a pronounced increase in mitochondrial ROS and a decrease in mitochondrial membrane potential, whereas simultaneous overexpression of *USP7* partially reversed these alterations (Fig. 8**G–J**). Taken together, these data demonstrate that *USP7* overexpression can attenuate the pro-ferroptotic effects driven by *METTL14* upregulation in a cellular model of SCI.

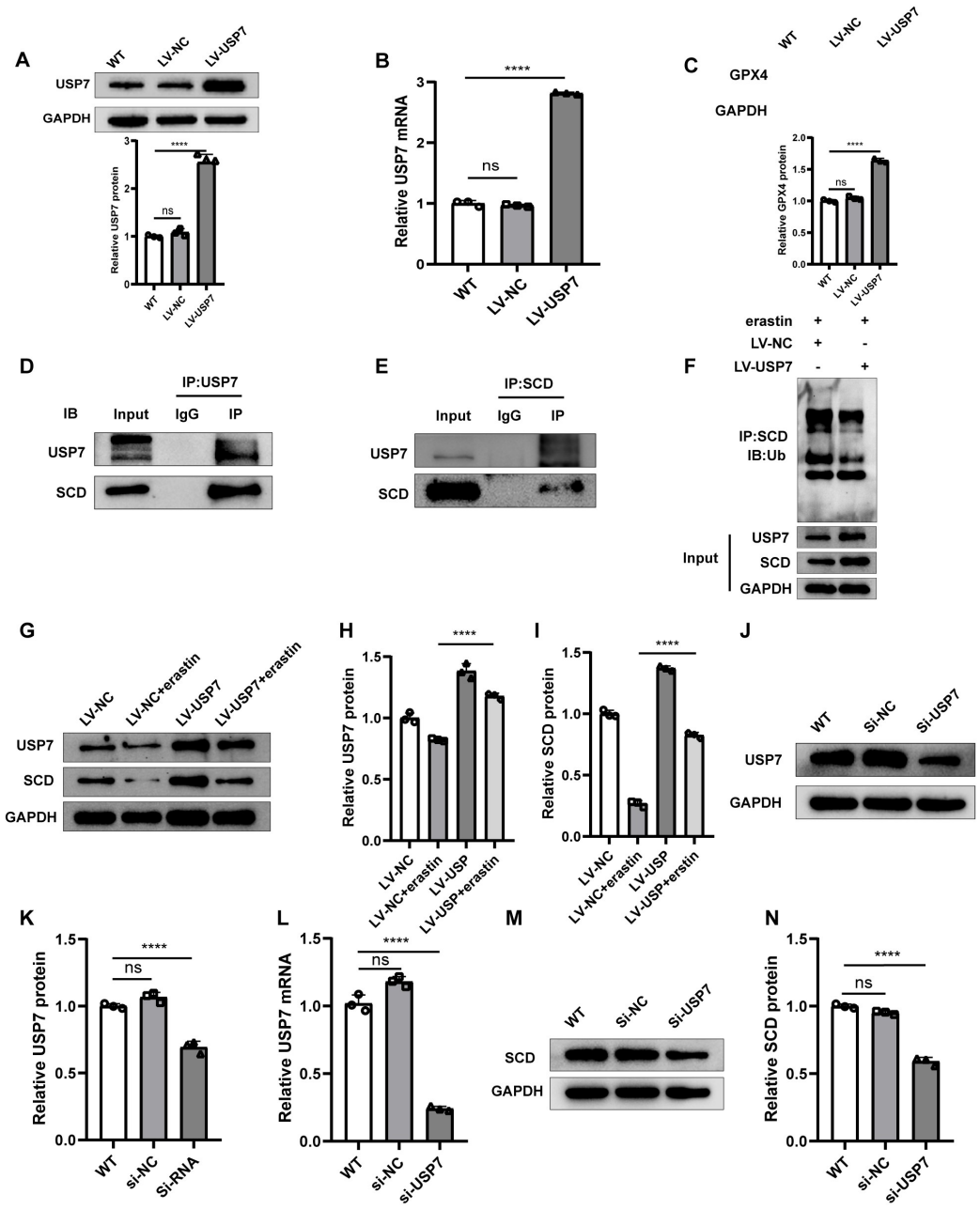


Fig. 7. ***USP7*** **regulates SCD expression through deubiquitination in ferroptosis.** (**A,B**) Expression of *USP7* by Western blot and RT-qPCR in PC12 cells. (**C**) Expression of *GPX4* by Western blot. (**D,E**) Co-immunoprecipitation (Co-IP) was used to detect the binding of *USP7* and *SCD*. (**F**) The ubiquitination level of *SCD* in PC12 cells. (**G–I**) Expression of *SCD* and *USP7* by Western blot in PC12 cells treated with erastin. (**J–L**) Expression of *USP7* by Western blot and RT-qPCR in PC12 cells transferred siRNA. (**M,N**) Expression of *SCD* was decreased when *USP7* inhibited in cells by Western blot. The data in the figures represent the means ± SD and analyzed using independent *t*-test. Significant differences between groups are indicated as ****$p < 0.0001$. The figures were drawn using Adobe Illustrator 2022.

Discussion

SCI represents a devastating neurological disorder with profound socioeconomic consequences worldwide [3]. Our study establishes ferroptosis characterized by iron-dependent lipid peroxidation as a pivotal pathological mechanism in SCI. We demonstrated that *METTL14* level and m6A content in SCI tissue were significantly increased, and the ferroptosis was activated. *METTL14* knockdown attenuates neuronal ferroptosis and mitigates SCI pathology by reducing m6A methylation of *USP7*. These findings highlight the *METTL14*/*USP7* pathway as a promising therapeutic target for inhibiting ferroptosis after SCI.

As the most prevalent RNA methylation modification in eukaryotes, m6A regulates diverse biological processes

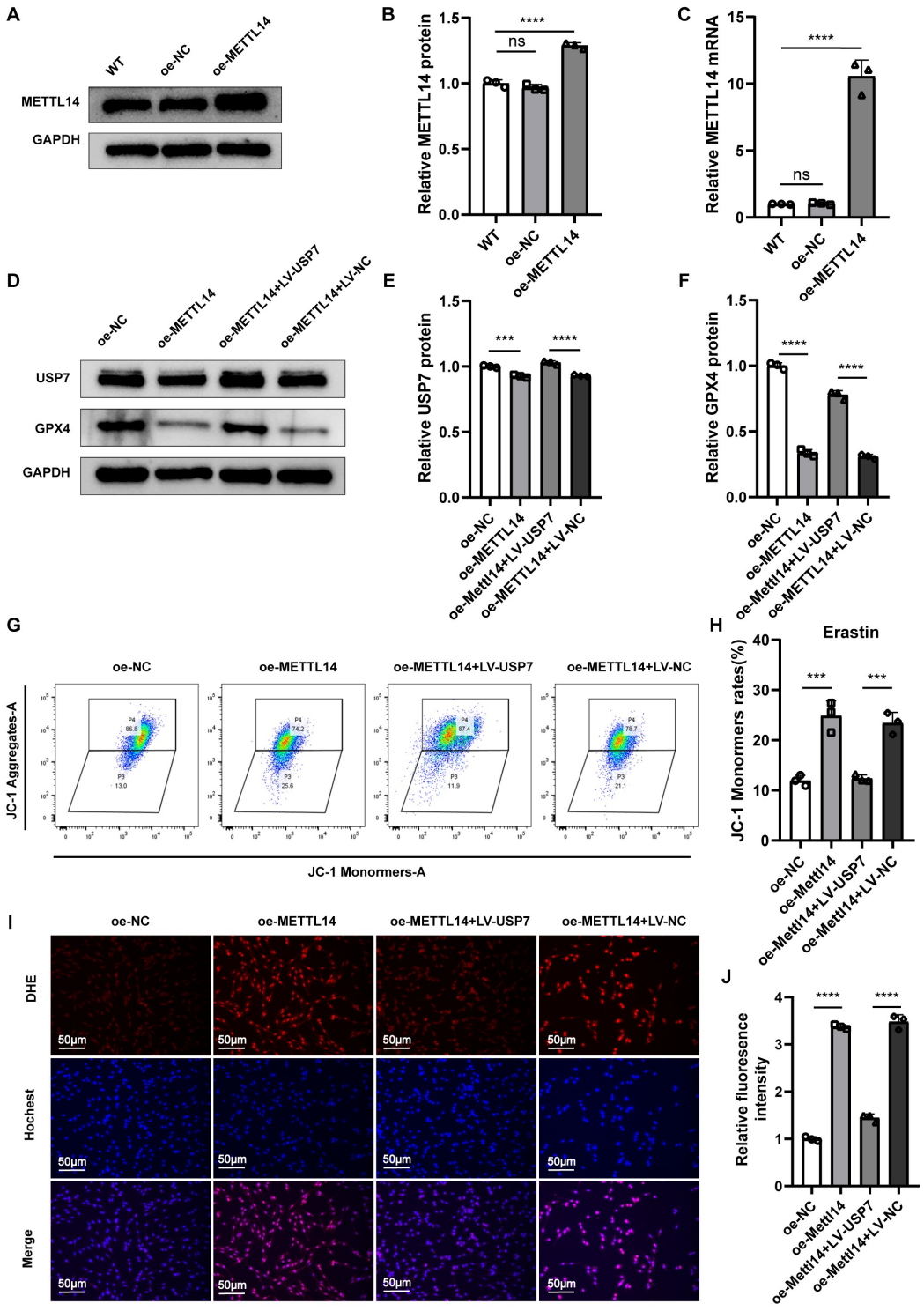


Fig. 8. Overexpression of *USP7* effectively counteracted the influence of *oe-METTL14* on the ferroptosis of SCI cells. (**A–C**) Expression of *METTL14* by Western blot and RT-qPCR in PC12 cells. (**D–F**) Expression of *GPX4* and *USP7* by Western blot. (**F**) The ubiquitination level of *SCD* in PC12 cells. (**G,H**) Mitochondrial membrane potential was evaluated by flow cytometry. (**I,J**) DHE staining and Hoechst staining. The data in the figures represent the means ± SD and analyzed using one-way ANOVA with Tukey's test. Significant differences between groups are indicated as $^{****}p < 0.0001$, $^{***}p < 0.001$. The figures were drawn using Adobe Illustrator 2022.

including stem cell maintenance and neuronal development [12]. Its dysregulation has been implicated in various neurological disorders and higher cognitive functions such as learning and memory [31,32]. In line with previous reports of elevated m6A levels in spinal cord neuronal apoptosis [21], we observed increased m6A methylation and

METTL14 expression in SCI tissues, accompanied by robust ferroptosis activation. Neurons exhibit particular susceptibility to ferroptosis due to their unique lipid composition and high oxidative metabolism [33]. Given the concurrent upregulation of *METTL14* and m6A in SCI, we investigated whether *METTL14* modulates neuronal ferroptosis through m6A-dependent mechanisms.

METTL14 silencing in SCI rats improved locomotor function (BBB scores) and inclined plane performance, ameliorated tissue pathology, and increased survival of anterior horn motor neurons. Consistently, *METTL14* knockdown reduced ferroptosis biomarkers including iron accumulation, MDA content, and *GPX4* depletion. While *METTL14* deletion has been shown to reduce m6A methylation and impair motor coordination, and while it ameliorates ferroptosis in acute pancreatitis [14], it promotes doxorubicin-induced cardiomyocyte ferroptosis via the *KCNQ1OT1-miR-7-5p-TFRC* axis [34]. Our results thus establish *METTL14* as a context-dependent regulator of ferroptosis in SCI.

Given the protective effects of *METTL14* deletion, we further explored its mechanism of action. *USP7*, a deubiquitinating enzyme involved in genomic stability maintenance through cell cycle regulation and DNA repair [35]. The stability of many proteins is dynamically governed by ubiquitination and deubiquitination cycles. Notably, the deubiquitinase *USP7* has been identified as a critical regulator of ferroptosis across multiple pathological contexts. Specifically, in a study of cardiac ischemia/reperfusion (I/R) injury, Tang *et al*. [36] reported that elevated levels of *USP7* were associated with increased expression of *p53* and *TfR1*, concomitant with enhanced ferroptosis. In addition, Guan *et al*. [22] confirmed its regulation of *SCD* stability by deubiquitination to promote ferroptosis in gastric cancer. But, its role in SCI remained unclear. In our study, bioinformatics revealed the m6A methylation modification sites of *USP7* mRNA, and there are interactions between *USP7* mRNA and *METTL14*. We used MeRIP to confirm the presence of m6A modification on *USP7* mRNA, inhibition of *METTL14* resulted in a significant decrease in m6A modification of *USP7*, suggesting that *METTL14* regulates the m6A modification of *USP7*. To assess the impact of *METTL14* on *USP7* mRNA stability, our experiments found that *METTL14* inhibition significantly increased *USP7* mRNA stability. To sum up, *METTL14* inhibition reduced *USP7* m6A methylation and enhanced its mRNA stability, thereby increasing *USP7* expression.

Evidences verified that *SCD* plays a pivotal role in ferroptosis is an iron-dependent nonapoptotic cell death mechanism triggered by increased accumulation of oxidized polyunsaturated fatty acids (PUFAs) and their subsequent incorporation into the phospholipid cell membrane [37]. *SCD*, an endoplasmic reticulum (ER) enzyme, catalyzes the △9-desaturation of saturated fatty acids (SFAs) to generate monounsaturated fatty acids (MUFAs), which are less susceptible to peroxidation. Consequently, *SCD* upregulation enhances cellular resistance to ferroptosis by increasing MUFA production. Conversely, *SCD* inhibition depletes this protective pool of MUFAs, sensitizing cells to ferroptosis and its inducers [38,39]. These researches indicate that *SCD* plays a crucial role in regulating lipid peroxidation and ferroptosis. In our study, after silencing *METTL14* expression, *USP7* and *SCD* level increased significantly. Co-IP experiments demonstrated that *USP7* could bind and deubiquitinates *SCD*. *USP7* overexpression reduced the ubiquitination level of *SCD* and improved expression of *SCD*. These results suggesting that *USP7* decreases *SCD* ubiquitination, likely through removal of K48-linked chains, though further linkage-specific assays are required. In addition, upregulated *USP7* reduced iron accumulation, MDA levels, and mitochondrial damage while increasing GSH and *GPX4* expression in erastin-treated cells. These results align with *SCD*'s known role in inhibiting lipid peroxidation and its involvement in neuronal survival and regeneration [40]. To sum up, our findings support a model in which *METTL14* depletion reduces m6A methylation, stabilizes *USP7* mRNA, enhances *USP7*-mediated *SCD* deubiquitination, and ultimately suppresses ferroptosis. To our knowledge, this is the first systematic demonstration to delineate the *METTL14*/m6A/*USP7* regulatory axis in neuronal ferroptosis following SCI. As the *METTL14–USP7–SCD* axis is further explored in the treatment of SCI, it provides a theoretical basis for the application of drugs, such as *METTL14* inhibitors or *USP7* activators.

This study has several limitations. First, we did not systematically validate other potential downstream targets of *METTL14* or explore alternative regulatory pathways. Second, more comprehensive *in vivo* evidence: such as cell-type-specific knockout models, is needed to fully establish the relationship between *SCD* and ferroptosis in SCI. Although our *in vitro* rescue experiment supports the *METTL14–USP7–SCD* axis, an *in vivo* genetic rescue would be required to fully establish the causal chain in the intact spinal cord environment. Moreover, enzymatic activity of *USP7* and ubiquitin linkage type between *USP7* and *SCD* are worthwhile to conduct deeper research. Although our MeRIP-qPCR and bioinformatic analyses suggest that *METTL14* mediates m6A modification of *USP7* mRNA, direct validation would require site-directed mutagenesis of the predicted adenosine residues within the putative m6A motifs. Mutation of these sites would be expected to abolish *METTL14*-induced *USP7* mRNA degradation. This represents an important direction for future investigations to pinpoint the exact m6A sites responsible for the observed regulation. Future studies will address these aspects to further elucidate the mechanistic network underlying ferroptosis regulation in neural injury.

Conclusions

In summary, this study demonstrates that *METTL14* is significantly upregulated following SCI and that its suppression effectively inhibits ferroptosis in spinal neurons. Mechanistically, *METTL14* knockdown enhances *USP7* expression by reducing m6A-mediated mRNA decay, thereby attenuating ferroptotic cell death and mitigating SCI progression. Our findings reveal a previously unrecognized *METTL14–USP7* regulatory axis, highlighting its potential as a therapeutic target for SCI. Further investigation is warranted to fully elucidate the underlying mechanisms and evaluate the translational feasibility of targeting this pathway.

List of Abbreviation

SCI, Spinal cord injury; NSCs/NPCs, Neural stem/progenitor cells; MSCs, Mesenchymal stem cells; iPSCs, Induced pluripotent stem cells; m6A, N6-methyladenosine; *METTL14*, Methyltransferase-like 14; DUBs, Deubiquitinating enzymes; *USP7* (HAUSP), Ubiquitin-specific protease 7; *METTL3*, Methyltransferase-like 3; *SCD*, Stearoyl-CoA desaturase; NC, Negative control; BBB, Basso, Beattie, Bresnahan; IPT, Inclined plane test; RT-qPCR, Reverse transcription-quantitative polymerase chain reaction; HE, hematoxylin and eosin; BCA assay kit, bicinchoninic acid assay kit; SDS-PAGE, Sodium dodecyl sulfate-polyacrylamide gel electrophoresis; PVDF, Polyvinylidene fluoride; *GPX4*, Glutathione peroxidase 4; *ACSL4*, Acyl-CoA synthetase long chain family member 4; *GAPDH*, Glyceraldehyde-3-phosphate dehydrogenase; PBS, Phosphate Buffered Saline; RPMI 1640 medium, Roswell Park Memorial Institute-1640 medium; CCK-8, Cell Counting Kit-8; DMSO, Dimethyl sulfoxide; MDA, Malondialdehyde; GSH, Glutathione; TEM, Transmission electron microscopy; LV, Lentivirus; siRNA, Small interfering RNA; DHE, Dihydroethidium; ROS, Reactive Oxygen Species; Co-IP, Co-immunoprecipitation; SFAs, Saturated fatty acids; MUFAs, Monounsaturated fatty acids; AAV, Adeno-Associated Virus; ER, endoplasmic reticulum; ANOVA, analysis of variance; SD, standard deviation; I/R, ischemia/reperfusion.

Availability of Data and Materials

The original data is available from the corresponding authors.

Author Contributions

KW: Writing—original draft, Validation, Resources, Methodology, Investigation, Data curation. JBW and YCZ: Software, Project administration, Methodology, Formal analysis, Conceptualization. DWC, JW, FLW: Investigation, Data curation, Formal analysis. ZQZ: Visualization, Supervision. CSW: Writing—review & editing, Visualization, Supervision, Funding acquisition.

Ethics Approval and Consent to Participate

All animal experiments were approved by the Animal Ethics Committee of Fujian Medical University (No. IACUC FJMU 2025-0183) and were performed according to the National Institute of Health Guide for the Care and Use of Laboratory Animals.

Acknowledgments

Thanks for all the contributors.

Funding

This work was supported by the Fujian Provincial Health Technology Project (Project number: 2022CXA023) and the Joint Funds for the Innovation of Science and Technology, Fujian Province (Project number: 2021Y9147).

Conflict of Interest

The authors declare no conflict of interest.

References

[1] Anjum A, Yazid MD, Fauzi Daud M, Idris J, Ng AMH, Selvi Naicker A, *et al*. Spinal Cord Injury: Pathophysiology, Multimolecular Interactions, and Underlying Recovery Mechanisms. International Journal of Molecular Sciences. 2020; 21: 7533. https://doi.org/10.3390/ijms21207533.

[2] Hamid R, Averbeck MA, Chiang H, Garcia A, Al Mousa RT, Oh SJ, *et al*. Epidemiology and pathophysiology of neurogenic bladder after spinal cord injury. World Journal of Urology. 2018; 36: 1517–1527. https://doi.org/10.1007/s00345-018-2301-z.

[3] Yamazaki K, Kawabori M, Seki T, Houkin K. Clinical Trials of Stem Cell Treatment for Spinal Cord Injury. International Journal of Molecular Sciences. 2020; 21: 3994. https://doi.org/10.3390/ijms21113994.

[4] Bertolo A, Sonntag S, Nyfeler N, Satkunaseelan S, Buergin J, Haumer A, *et al*. Minimally manipulated autologous cell therapy for pressure injury management in spinal cord injury: an in vitro seminal study. European Cells & Materials. 2025; 54: 31–47. https://doi.org/10.22203/eCM.v054a03.

[5] Zha X. Bioinformatics analysis techniques identify the ferroptosis-related gene MYCas a potential therapeutic target for spinal cord injury: an observational study based on the GEO database. Advanced Technology in Neuroscience. 2025; 2: 59–71. https://doi.org/10.4103/ATN.ATN-D-24-00026.

[6] Shi Z, Yuan S, Shi L. Programmed cell death in spinal cord injury pathogenesis and therapy. Cell Proliferation. 2021; 54: e12992. https://doi.org/10.1111/cpr.12992.

[7] Hirschhorn T, Stockwell BR. The development of the concept of ferroptosis. Free Radical Biology and Medicine. 2019; 133: 130–143. https://doi.org/10.1016/j.freeradbiomed.2018.09.043.

[8] Li QS, Jia YJ. Ferroptosis: a critical player and potential therapeutic target in traumatic brain injury and spinal cord injury. Neural Regeneration Research. 2023; 18: 506–512. https://doi.org/10.4103/1673-5374.350187.

[9] Zhang Y, Sun C, Zhao C, Hao J, Zhang Y, Fan B, *et al*. Ferroptosis inhibitor SRS 16-86 attenuates ferroptosis and promotes functional recovery in contusion spinal cord injury. Brain Research. 2019; 1706: 48–57. https://doi.org/10.1016/j.brainres.2018.10.023.

[10] Kang Y, Li Q, Zhu R, Li S, Xu X, Shi X, *et al*. Identification of Ferroptotic Genes in Spinal Cord Injury at Different Time Points: Bioinformatics and Experimental Validation. Molec-

ular Neurobiology. 2022; 59: 5766–5784. https://doi.org/10.1007/s12035-022-02935-y.
[11] Xiang M, Liu W, Tian W, You A, Deng D. RNA N-6-methyladenosine enzymes and resistance of cancer cells to chemotherapy and radiotherapy. Epigenomics. 2020; 12: 801–809. https://doi.org/10.2217/epi-2019-0358.
[12] Frye M, Harada BT, Behm M, He C. RNA modifications modulate gene expression during development. Science. 2018; 361: 1346–1349. https://doi.org/10.1126/science.aau1646.
[13] Li L, Zeng J, He S, Yang Y, Wang C. METTL14 decreases FTH1 mRNA stability via m6A methylation to promote sorafenib-induced ferroptosis of cervical cancer. Cancer Biology & Therapy. 2024; 25: 2349429. https://doi.org/10.1080/15384047.2024.2349429.
[14] Chen F, Su M, Han D, Wang Y, Song M. METTL14 depletion ameliorates ferroptosis in severe acute pancreatitis by increasing the N6-methyladenosine modification of ACSL4 and STA1. International Immunopharmacology. 2024; 128: 111495. https://doi.org/10.1016/j.intimp.2024.111495.
[15] Lu Z, Liu H, Song N, Liang Y, Zhu J, Chen J, *et al*. METTL14 aggravates podocyte injury and glomerulopathy progression through N6-methyladenosine-dependent downregulating of Sirt1. Cell Death & Disease. 2021; 12: 881. https://doi.org/10.1038/s41419-021-04156-y.
[16] Huang J, Dong X, Gong Z, Qin LY, Yang S, Zhu YL, *et al*. Solution structure of the RNA recognition domain of METTL3-METTL14 N^6-methyladenosine methyltransferase. Protein & Cell. 2019; 10: 272–284. https://doi.org/10.1007/s13238-018-0518-7.
[17] Jian D, Wang Y, Jian L, Tang H, Rao L, Chen K, *et al*. METTL14 aggravates endothelial inflammation and atherosclerosis by increasing FOXO1 N6-methyladenosine modifications. Theranostics. 2020; 10: 8939–8956. https://doi.org/10.7150/thno.45178.
[18] Dewson G, Eichhorn PJA, Komander D. Deubiquitinases in cancer. Nature Reviews Cancer. 2023; 23: 842–862. https://doi.org/10.1038/s41568-023-00633-y.
[19] Zong Z, Zhang Z, Wu L, Zhang L, Zhou F. The Functional Deubiquitinating Enzymes in Control of Innate Antiviral Immunity. Advanced Science. 2020; 8: 2002484. https://doi.org/10.1002/advs.202002484.
[20] Liu B, Ruan J, Chen M, Li Z, Manjengwa G, Schlüter D, *et al*. Deubiquitinating enzymes (DUBs): decipher underlying basis of neurodegenerative diseases. Molecular Psychiatry. 2022; 27: 259–268. https://doi.org/10.1038/s41380-021-01233-8.
[21] Guo S, Lin T, Chen G, Shangguan Z, Zhou L, Chen Z, *et al*. METTL3 Affects Spinal Cord Neuronal Apoptosis by Regulating Bcl-2 m6A Modifications After Spinal Cord Injury. Neurospine. 2023; 20: 623–636. https://doi.org/10.14245/ns.2346170.085.
[22] Guan X, Wang Y, Yu W, Wei Y, Lu Y, Dai E, *et al*. Blocking Ubiquitin-Specific Protease 7 Induces Ferroptosis in Gastric Cancer via Targeting Stearoyl-CoA Desaturase. Advanced Science. 2024; 11: e2307899. https://doi.org/10.1002/advs.202307899.
[23] Breuer S, Pech K, Buss A, Spitzer C, Ozols J, Hol EM, *et al*. Regulation of stearoyl-CoA desaturase-1 after central and peripheral nerve lesions. BMC Neuroscience. 2004; 5: 15. https://doi.org/10.1186/1471-2202-5-15.
[24] Wang P, Doxtader KA, Nam Y. Structural Basis for Cooperative Function of Mettl3 and Mettl14 Methyltransferases. Molecular Cell. 2016; 63: 306–317. https://doi.org/10.1016/j.molcel.2016.05.041.
[25] Hao J, Li B, Duan HQ, Zhao CX, Zhang Y, Sun C, *et al*. Mechanisms underlying the promotion of functional recovery by deferoxamine after spinal cord injury in rats. Neural Regeneration Research. 2017; 12: 959–968. https://doi.org/10.4103/1673-5374.208591.
[26] Yao S, Pang M, Wang Y, Wang X, Lin Y, Lv Y, *et al*. Mesenchymal stem cell attenuates spinal cord injury by inhibiting mitochondrial quality control-associated neuronal ferroptosis. Redox Biology. 2023; 67: 102871. https://doi.org/10.1016/j.redox.2023.102871.
[27] Xu Q, Kong F, Zhao G, Jin J, Feng S, Li M. USP7 alleviates neuronal inflammation and apoptosis in spinal cord injury via deubiquitinating NRF1/KLF7 axis. Neurological Research. 2024; 46: 1008–1017. https://doi.org/10.1080/01616412.2024.2376999.
[28] Sen U, Coleman C, Sen T. Stearoyl coenzyme A desaturase-1: multitasker in cancer, metabolism, and ferroptosis. Trends in Cancer. 2023; 9: 480–489. https://doi.org/10.1016/j.trecan.2023.03.003.
[29] Kubota CS, Espenshade PJ. Targeting Stearoyl-CoA Desaturase in Solid Tumors. Cancer Research. 2022; 82: 1682–1688. https://doi.org/10.1158/0008-5472.CAN-21-4044.
[30] Zhang Y, Gu Z, Wan J, Lou X, Liu S, Wang Y, *et al*. Stearoyl-CoA Desaturase-1 dependent lipid droplets accumulation in cancer-associated fibroblasts facilitates the progression of lung cancer. International Journal of Biological Sciences. 2022; 18: 6114–6128. https://doi.org/10.7150/ijbs.74924.
[31] Satterlee JS, Basanta-Sanchez M, Blanco S, Li JB, Meyer K, Pollock J, *et al*. Novel RNA modifications in the nervous system: form and function. The Journal of neuroscience: the official journal of the Society for Neuroscience. 2014; 34: 15170–15177. https://doi.org/10.1523/JNEUROSCI.3236-14.2014.
[32] Koranda JL, Dore L, Shi H, Patel MJ, Vaasjo LO, Rao MN, *et al*. Mettl14 Is Essential for Epitranscriptomic Regulation of Striatal Function and Learning. Neuron. 2018; 99: 283–292.e5. https://doi.org/10.1016/j.neuron.2018.06.007.
[33] Zou Y, Henry WS, Ricq EL, Graham ET, Phadnis VV, Maretich P, *et al*. Plasticity of ether lipids promotes ferroptosis susceptibility and evasion. Nature. 2020; 585: 603–608. https://doi.org/10.1038/s41586-020-2732-8.
[34] Zhuang S, Ma Y, Zeng Y, Lu C, Yang F, Jiang N, *et al*. METTL14 promotes doxorubicin-induced cardiomyocyte ferroptosis by regulating the KCNQ1OT1-miR-7-5p-TFRC axis. Cell Biology and Toxicology. 2023; 39: 1015–1035. https://doi.org/10.1007/s10565-021-09660-7.
[35] Valles GJ, Bezsonova I, Woodgate R, Ashton NW. USP7 Is a Master Regulator of Genome Stability. Frontiers in Cell and Developmental Biology. 2020; 8: 717. https://doi.org/10.3389/fcell.2020.00717.
[36] Tang LJ, Zhou YJ, Xiong XM, Li NS, Zhang JJ, Luo XJ, *et al*. Ubiquitin-specific protease 7 promotes ferroptosis via activation of the p53/TfR1 pathway in the rat hearts after ischemia/reperfusion. Free Radical Biology and Medicine. 2021; 162: 339–352. https://doi.org/10.1016/j.freeradbiomed.2020.10.307.
[37] Wohlhieter CA, Richards AL, Uddin F, Hulton CH, Quintanal-Villalonga À, Martin A, *et al*. Concurrent Mutations in STK11 and KEAP1 Promote Ferroptosis Protection and SCD1 Dependence in Lung Cancer. Cell Reports. 2020; 33: 108444. https://doi.org/10.1016/j.celrep.2020.108444.
[38] Wang C, Shi M, Ji J, Cai Q, Zhao Q, Jiang J, *et al*. Stearoyl-CoA desaturase 1 (SCD1) facilitates the growth and anti-ferroptosis of gastric cancer cells and predicts poor prognosis of gastric cancer. Aging. 2020; 12: 15374–15391. https://doi.org/10.18632/aging.103598.
[39] Chen L, Hambright WS, Na R, Ran Q. Ablation of the Ferroptosis Inhibitor Glutathione Peroxidase 4 in Neurons Results in Rapid Motor Neuron Degeneration and Paralysis. The Journal of Biological Chemistry. 2015; 290: 28097–28106. https://doi.org/10.1074/jbc.M115.680090.
[40] Stockwell BR, Friedmann Angeli JP, Bayir H, Bush AI, Conrad M, *et al*. Ferroptosis: A Regulated Cell Death Nexus Linking Metabolism, Redox Biology, and Disease. Cell. 2017; 171: 273–285. https://doi.org/10.1016/j.cell.2017.09.021.

Editor's note: The Scientific Editors responsible for this paper were Xiaolei Zhang and Martin Stoddart.

Received: 7th December 2025; **Accepted**: 31th August 2026; **Published**: 30th October 2026